

# Implications for explosion mechanism of SNe Ia from late-time spectra(a crude and temporary title)

JIALIAN LIU<sup>1</sup>

<sup>1</sup>*Physics Department, Tsinghua University, Beijing 100084, China*

## ABSTRACT

The late-time spectra of Type Ia Supernovae (SNe Ia) are important in studying the physics of their explosions. We have collected published late-time optical spectra of 32 SNe Ia at  $\sim 200 - 400$  days after peak magnitude. We also publish two new such late-time spectra of SN 2021hpr in this study. At this phase, the outer ejector has become transparent and the features of inner iron-group elements can be found in the spectra. We use multi-component Gaussian fits to measured the widths, velocity shifts and strengths of iron and nickel features. Then we estimate the nebular velocities and Ni/Fe ratios. We find that the number of SNe Ia which have a redshifted nebular velocity or a blueshifted nebular velocity is similar in our sample. Besides, the majority of SNe Ia are in favor of Sub- $M_{ch}$  models. We also try to find some connections between these late-time parameters and the early-time observations. The correlations imply that the observed velocity shift of Si II 6355 Å at maximum light increases with higher metallicity and is affected by the viewing angle due to asymmetric explosions.

*Keywords:* supernovae — general-methods — statistical

## 1. INTRODUCTION

It is widely accepted that type Ia supernovae (SNe Ia; see, e.g. [Filippenko 1997](#) for a review of supernova classification) result from thermonuclear explosion of a carbon-oxygen (CO) white dwarf ([Nomoto et al. 1997a](#); [Hillebrandt & Niemeyer 2000](#); [Maoz et al. 2014](#)). Proposed explosion scenarios are generally split into two progenitor systems: the single-degenerate scenario ([Whelan & Iben 1973](#)) with accretion-induced explosion of a massive WD with a non-degenerate companion, and the double-degenerate ([Iben & Tutukov 1984](#); [Webbink 1984](#)) scenario with merger-induced explosion of two white dwarfs. Numerical explosion models for explosion scenarios were proposed, such as the  $M_{ch}$  W7 models of [Nomoto et al. \(1997b\)](#) and [Iwamoto et al. \(1999\)](#), the  $M_{ch}$  DDT models of [Seitenzahl et al. \(2013\)](#), and the sub- $M_{ch}$  detonation models of [Sim et al. \(2010\)](#) and [Shen et al. \(2018\)](#). However, none of the models entirely succeed to be consistent with observations. We still do not understand the explosion mechanism well.

Spectra of SNe Ia are important in studying the explosion mechanism. Many useful parameters can be obtained from the early-time spectra. The postmaximum

decline rate  $\Delta m_{15}(B)$ , the decline in magnitudes in the B band during the first 15 days postmaximum, has a correlation with peak luminosity that brighter objects have a lower  $\Delta m_{15}(B)$  than the dimmer ones ([Phillips 1993](#); [Phillips et al. 1999](#)). The velocity shift of Si II 6355 Å absorption can be used to deduce the photospheric velocity, which gives a direct indication of the kinetic energy of the explosion. However, the outer ejecta is opaque at early time and the information of the inner ejecta is hidden. At phase of about more than 200 days after peak magnitude, the outer ejecta become transparent and the inner region dominated by iron-group elements is visible. Figure 1 shows an example of such late-time spectra. The 7300 Å region, dominated by [Fe II] and [Ni II] features (e.g., [Maguire et al. 2018](#); [Flörs et al. 2020](#)), is important to measured the nebular velocity which can be used to study explosion asymmetry (e.g., [Maeda et al. 2010a](#); [Silverman et al. 2013](#); [Maguire et al. 2018](#)). Besides, Ni/Fe ratio inferred from the 7300 Å region is used to constrain the explosion models in recent studies (e.g., [Maguire et al. 2018](#); [Flörs et al. 2020](#); [Graham et al. 2022](#)), since sub- $M_{ch}$  models predict a lower Ni/Fe ratio compared with  $M_{ch}$  models unless the metallicity of the progenitor is high enough. The connection between the Si II velocities (or velocity gradients) at maximum light and the nebular velocities of SNe Ia has been discussed in many works (e.g., [Maeda et al. 2010a](#)).

However, other connections between observations near maximum light and late-time observations seem to be rarely mentioned.

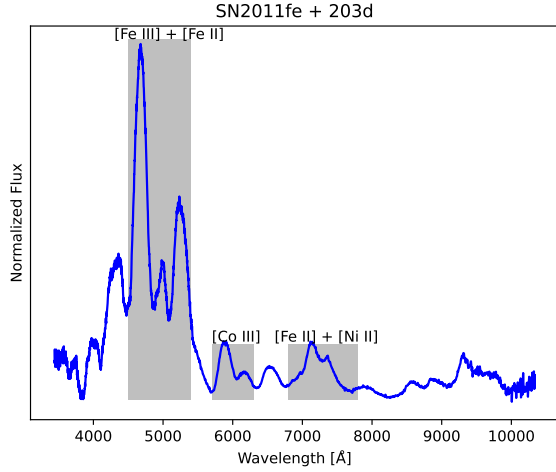


**Figure 1.** Spectrum of SN 2011fe from 203 d past maximum brightness. Some prominent features are labelled by shaded areas.

This work mainly attempts to study the potential correlations between early-time observations (the Si II velocity at maximum light and  $\Delta m_{15}(B)$ ) and late-time observations (the nebular velocity and Ni/Fe ratio). We outline our data sources in Section 2. In Section 3, we show the fitting methods and how we roughly estimate the Ni/Fe ratio. Our results are presented in section 4 and the findings are discussed in Section 5. Then we give our conclusions in Section 6.

## 2. DATA SOURCE

In order to study the distribution of Ni to Fe ratio for SNe Ia, we collect a sample of 52 late-time spectra ( $\sim 200$ -430 d) of 33 SNe Ia. Peculiar 91T-like and 91bg-like SNe Ia are included except for those exhibiting strong calcium features at late time. The publicly available data were retrieved using the Open Supernova Catalog (OSC, [Guillochon et al. 2017](#)), Weizmann Interactive Supernova data REpository (WiSeREP, [Yaron & Gal-Yam 2012](#)) and Supernovae Database (SNDB, [Stahl et al. 2020](#)), along with spectra of SN 2017fgc ([Zeng et al. 2021](#)), SN 2019ein (Xi, in prep), SN 2019np (Sai, in prep) and SN 2021hpr (This work). To study the connection between early-time observations and late-time observations, we have collected Si II velocities at maximum light and post-maximum decline rates  $\Delta m_{15}(B)$  of these SNe Ia from literatures. To correct the reddening

of the spectra, we have also collected redshift from WiSeREP and extinction from literatures. All these parameters and references are listed in Table A1. The references of spectra can be found in Table A3.  $R_v$  are assumed to be 3.1 except those listed in Table A2. The results should be little affected by the extinction, since we only focus on the 7300 Å region.

### 2.1. SN 2021hpr

We present 2 new late-time spectra of SN 2021hpr taken with the Lick-3m telescope. An overview of the observations for this supernovae is given in Table 1.

Lick-3m

## 3. METHOD

### 3.1. Fitting methods

We focus on the 7300 Å region which ranges about 6800 - 7800 Å and is dominated by [Fe II] (7155, 7172, 7388, 7453 Å) and [Ni II] (7378, 7412 Å) ([Maguire et al. 2018](#)). We use a multi-component Gaussian function to fit this region. Here we briefly summarize the processes of the fits. Each spectrum first is corrected for redshift and extinction according to the values presented in Table A1, and then is smoothed with a Savitsky-Golay filter using the `scipy` package's `signal.savgol_filter` function. The window size of the filter ranges about 30 - 200 Å depending on the signal-to-noise of the spectra. The fit region should be chosen carefully to obtain a reasonable result. Generally, the local minimum near about 6800 Å is set to be the blue endpoint. The blue endpoint chosen in this way may induce some flux excess in the blue side of the features, which may be due to [Co III] emissions ([Flörs et al. 2020](#)). Figure 2 shows the evolution of the flux excess for SN 2011fe, SN2012fr and SN 2014J. It is easy to find that the excess decreases with time and nearly disappears at +350 d, which can be due to the decay of cobalt. The red side of the features near  $\sim 7600$  Å is usually polluted by absorption features that may come from the earth atmosphere, so we choose a point redder than the absorption feature as the red endpoint. Distinct excess in the blue side and absorption features in the red side would be removed from the fit region. The pseudo-continuum is defined as a straight line connecting the red and blue endpoints of the fit region. Subtracting the continuum, the `scipy.optimize.curve_fit` function is used to fit a multi-component Gaussian function to the features. We follow the fit of [Maguire et al. \(2018\)](#) that the widths and velocity shifts of the lines of the same element are set to the same value and the relative strengths of the same element are fixed. We use

**Table 1.** Overview of the observations.

Name	Observation	Observation	Phase	$E(B - V)$	redshift	Host galaxy	Exposure
	MJD	date		(mag)			
SN 2021hpr	59585	2022 Jan 6	+290d	$0.098 \pm 0.06$	0.009346	NGC 3147	

the value of [Jerkstrand et al. \(2015\)](#), where [Fe II] 7172, 7388, 7453 Å features have relative strengths of 0.24, 0.19, 0.31 compared to the [Fe II] 7155 Å feature and the [Ni II] 7412 Å feature have a relative strength of 0.31 compared to the [Ni II] 7378 Å feature. Then there are only 6 free parameters for the multi-component Gaussian function, namely, the widths, velocity shifts and strengths of [Fe II] 7155 Å and [Ni II] 7378 Å features. The FWHM of [Ni II] 7378 Å is limited to be less than  $13000 \text{ km s}^{-1}$ , which is adopted by [Graham et al. \(in prep\)](#) to avoid overly-broad-and-shallow nickel features being fit. In practice, we find that overly-broad nickel features would appear when iron features cannot satisfy the region ranges about 7200 - 7300 Å. We can adjust the fit region to avoid overly-broad nickel features in most cases. When the adjustment doesn't work, we try to remove the  $\sim 7200 - 7300$  Å region. Figure 3 shows two examples of how we avoid overly-broad nickel features.

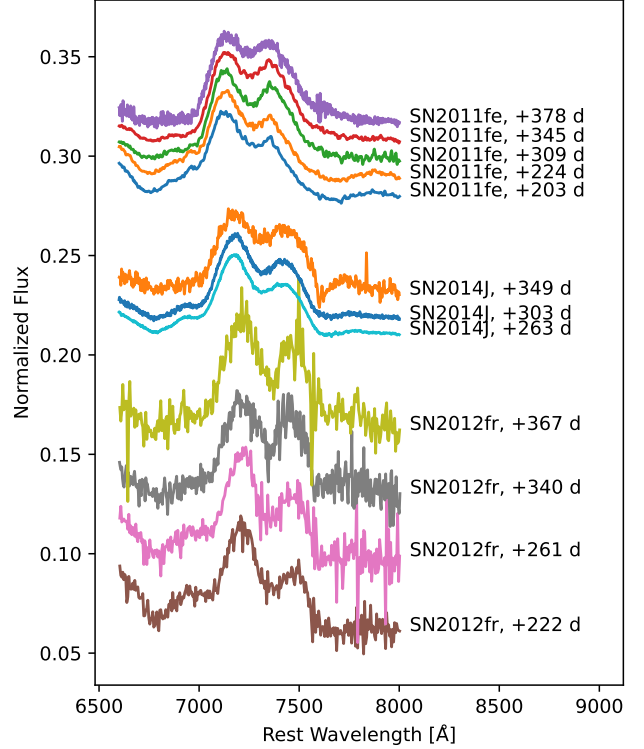
To estimate the uncertainties, we shift the edges of the fit region within 50 Å (in some low signal-to-noise cases, this is reduced to 10 Å) and re-fit 1000 times. If the flux excess in the red side or the absorption features are removed from the fit region, we also shift the edges of them within 10 Å. A bad fit will be rejected, for example, when the width of Ni is close to  $13000 \text{ km s}^{-1}$ . The standard deviation in the measurements is taken as one of the errors of the Gaussian parameters. Another error comes from the smoothing of the spectrum, which we estimate as the difference between the results given by the smoothed spectrum and the primary spectrum. We also add an uncertainty on the velocity shift measurements of  $200 \text{ km s}^{-1}$  to account for peculiar velocity effects of the host galaxies ([Maguire et al. 2018](#)).

### 3.2. Rough nickel-to-iron ratio

The nickel-to-iron ratio is estimated following the method of [Maguire et al. \(2018\)](#),

$$\frac{n_{\text{Ni II}}}{n_{\text{Fe II}}} = \frac{L_{7378}}{L_{7155}} \exp\left(-\frac{0.28}{kT}\right) \frac{d_{C_{\text{Fe II}}}}{d_{C_{\text{Ni II}}}} / 4.9 \quad (1)$$

where  $\frac{d_{C_{\text{Fe II}}}}{d_{C_{\text{Ni II}}}}$  is the departure coefficients,  $\frac{L_{7378}}{L_{7155}}$  is the ratio of luminosity and estimated as the measured flux

**Figure 2.** Evolutions of flux excess in the blue side of the 7300 Å region.

ratio of [Fe II] 7155 Å and [Ni II] 7378 Å features,  $k$  is Boltzmann constant and  $T$  is the temperature.

To obtain a rough nickel-to-iron ratio, the departure coefficients  $\frac{d_{C_{\text{Fe II}}}}{d_{C_{\text{Ni II}}}}$  is assumed to be 1.8, the temperature is assumed to range from 3000K to 8000K and the nickel-to-iron ratio  $\frac{n_{\text{Ni}}}{n_{\text{Fe}}}$  is assumed to equal to  $\frac{n_{\text{Ni II}}}{n_{\text{Fe II}}}$ . The relative uncertainty of the nickel-to-iron ratio estimated in this way is about 40 percent and will be combined with the uncertainty of measured flux ratio to give a total uncertainty.

## 4. RESULTS

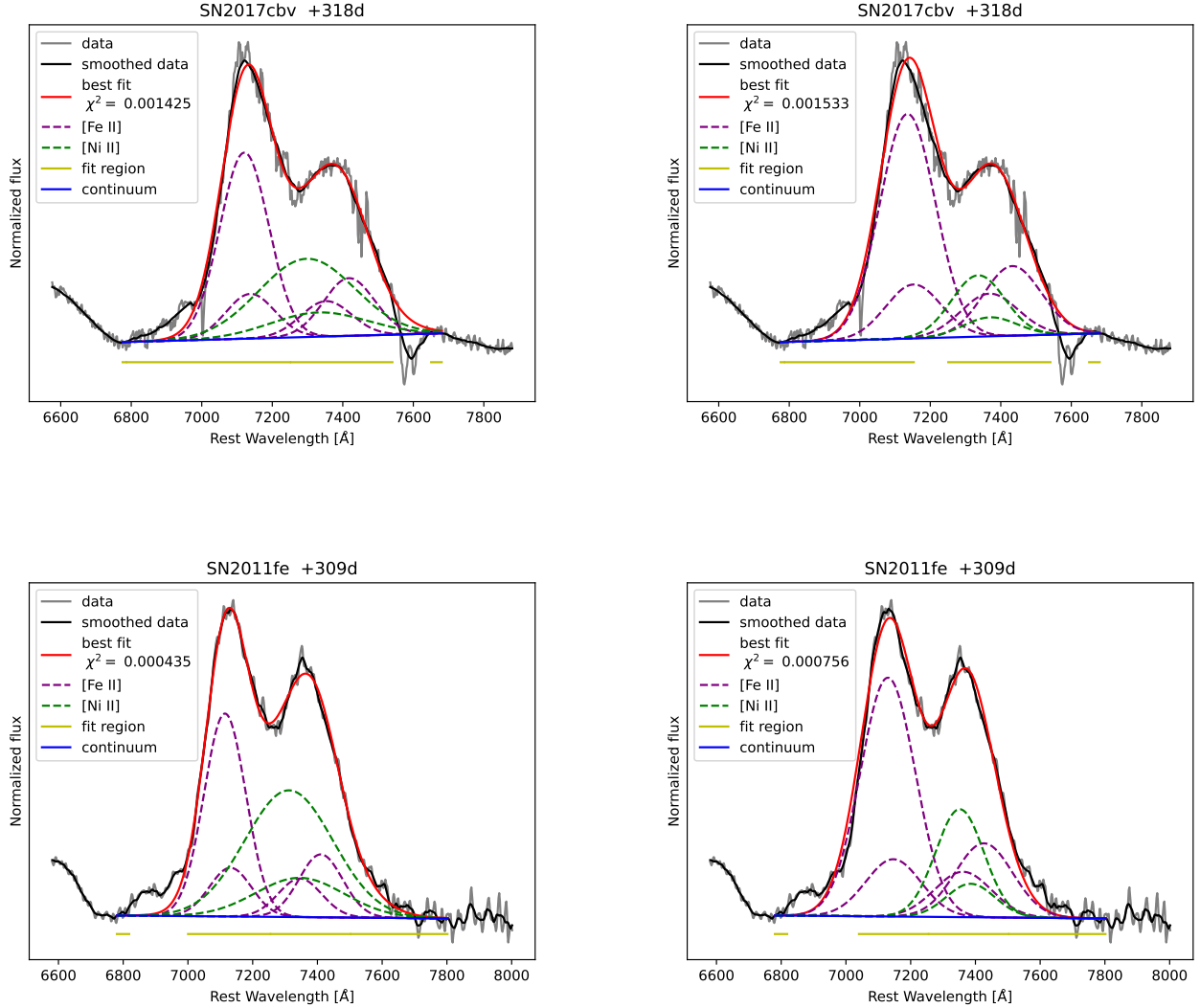


**Figure 3.** Some examples for our multi-component Gaussian fits. The reddening corrected observed spectra are shown in gray while the smoothed spectra are shown in black. The overall fits are shown in red, the [Fe II] features are showed in purple dashed lines and the [Ni II] features are showed in green dashed lines. The yellow lines show the region we choose to fit. The continuums are showed in blue. In the top panel, we adjust the fit region to avoid the overly broad nickel features. In the bottom panel, we remove some data points around 7200 Å to avoid the overly broad nickel features.

The FWHM and velocity shifts of [Fe II] 7155 Å and [Ni II] 7378 Å features as well as their flux ratios are listed in Table A3. We use the velocity shifts of [Fe II] 7155 Å and [Ni II] 7378 Å features to identify whether the nebular velocities are redshifted or blueshifted, which might have a connection with asymmetric explosion models (Maeda et al. 2010b). We use the flux ratio of [Fe II] 7155 Å and [Ni II] 7378 Å features to roughly estimate the Ni/Fe ratio and attempt to confine the explosion models. Inferred nebular velocities and Ni/Fe ratio are also listed in Table A3. Combining the nebular velocities and Ni/Fe ratios with the

Si II velocities at maximum light and post maximum decline rates  $\Delta m_{15}(B)$  presented in Table A1, we find some correlations between these late-time parameters and early-time parameters.

#### 4.1. Nebular velocities

The nebular velocity is estimated as the mean value of velocity shifts of [Fe II] 7155 Å and [Ni II] 7378 Å features (Maeda et al. 2010b). When the nebular velocity can be zero within the uncertainty, we do not identify whether it is redshifted or blueshifted and just consider the nebular velocity to be zero. We find 12 SNe

Ia have redshifted nebular velocities and 17 SNe Ia have blueshifted nebular velocities in our 33 SNe Ia samples in this way. The two SNe Ia classified by the nebular velocities have a similar number.

#### 4.2. Inferred Ni/Fe ratio

Figure 4 shows our roughly estimated mass ratio of Ni and Fe as a function of phase after maximum light. Shading regions mark the ranges of predictions for Ni/Fe ratio of different models and we find that the majority (about 2/3) of our SNe Ia samples are in agreement with a double detonation sub- $M_{Ch}$  model, which is also found by Flörs et al. (2020). The left SNe Ia are in agreement with a DDT model or have a critical Ni/Fe ratio between DDT models and sub- $M_{Ch}$  models, except SN 2015F and SN 2002bo whose inferred Ni/Fe ratio may be too high. The reason of the high Ni/Fe ratio of SN 2015F and SN 2002bo is unclear and these two SNe Ia are removed from the following analysis.

#### 4.3. Connection between the Ni-to-Fe ratio and the Si II velocity

For SNe Ia that have several spectra in this work, we choose the spectrum that is closest to 300 days after maximum light to do the analysis. Figure 5 shows the connection between the Ni/Fe ratio and the velocity of Si II 6355 Å at maximum light. We find that the Ni/Fe ratio increases with a higher Si II velocity at maximum for both the SNe Ia that have redshifted or blueshifted nebular velocities. The Si II velocity is lower than 12000  $\text{km s}^{-1}$  for the SNe Ia that have a blueshifted nebular velocity, while the Si II velocity can approach 16000  $\text{km s}^{-1}$  for the SNe Ia that have a redshifted nebular velocity. The range of Ni/Fe ratio is similar for these two SNe Ia. When the Si II velocity is low, about 10000  $\text{km s}^{-1}$ , the Ni/Fe ratio is similar for these two SNe Ia.

#### 4.4. Connection between the Ni/Fe ratio and $\Delta m_{15}(B)$

Figure 6 shows a comparison between the Ni/Fe ratio and  $\Delta m_{15}(B)$ . Different from Figure 5, red points and blue points are fully mixed. The Ni/Fe ratio increases with  $\Delta m_{15}(B)$  until  $\Delta m_{15}(B)$  become very large. When  $\Delta m_{15}(B)$  is very large, the Ni/Fe ratio become small and the corresponding point locates in the bottom right of the figure. However, where the transformation occurs is unclear, since we lack late-time spectra of SNe Ia that have a  $\Delta m_{15}(B)$  around 1.6 magnitude in this work.

### 5. DISCUSSIONS

We have used multi-component Gaussian fits to estimate the velocity shifts and flux ratios of late-time spectral features in the 7300 Å region for 33 SNe Ia samples

in this work. Nebular velocities and Ni/Fe ratios are inferred from the velocity shifts and the flux ratios respectively. Some relations are found between these inferred late-time parameters and the early-time parameters (Si II velocities at maximum light and  $\Delta m_{15}(B)$ ) in section 4. In this section, we discuss the implications for explosion mechanism from these relations. We also briefly discuss the possible contribution of Calcium in the 7300 Å region.

#### 5.1. Implications for explosion mechanism

Maeda et al. (2010b) find that the SNe Ia having high Si II velocity gradients ( $\gtrsim 70 \text{ km s}^{-1}$ ) display redshifted nebular velocities and propose an asymmetric and off-center explosion toy model to interpret this connection as geometric effect. Silverman et al. (2013) extend this connection and showed that velocity gradients can be replaced by Si II velocities at maximum light, namely, SNe Ia having high Si II velocities at maximum ( $\gtrsim 12000 \text{ km s}^{-1}$ ) display redshifted nebular velocities. Figure 5 shows that all the SNe Ia that have a high Si II velocity display a redshifted nebular velocity, which is in agreement with Silverman et al. (2013).

However, Wang et al. (2013) find that the SNe Ia with higher Si II velocity tend to occur nearer the galaxy centers where the stellar metallicity is higher. Wang et al. (2013) argue that the diversity of Si II velocities for SNe Ia cannot be completely attributed to geometric effect and the higher Si II velocity may be related in part to a higher metallicity environment. Our work also supports the findings of Wang et al. (2013). Timmes et al. (2003) describe how the ratio of stable-to-radioactive nucleosynthetic products increases with a higher-metallicity progenitor. A higher ratio of stable-to-radioactive nucleosynthetic products means a higher late-time Ni/Fe ratio since all the radioactive  $^{56}\text{Ni}$  would have decayed to  $^{56}\text{Co}$  and finally  $^{56}\text{Fe}$ . If we only focus on the SNe Ia that have a redshifted nebular velocity or that have a blueshifted nebular velocity, we find the Ni/Fe ratio increases with higher Si II velocity, namely, the metallicity of the progenitor has a positive correlation with the Si II velocity. This correlation is also in agreement with Lentz et al. (2000) that the blueward shift of the Si II feature increased with higher metallicity.

In our perspective, metallicity is one of the intrinsic sources of the diversity of Si II velocities while geometric effect caused by asymmetric explosion models affects the observed Si II velocity for the reasons that (1) Figure 5 shows two branches composed of red points (redshifted nebular velocity) and blue points (blueshifted nebular velocity) respectively. The numbers of red points and blue points are close, which implies that we may have



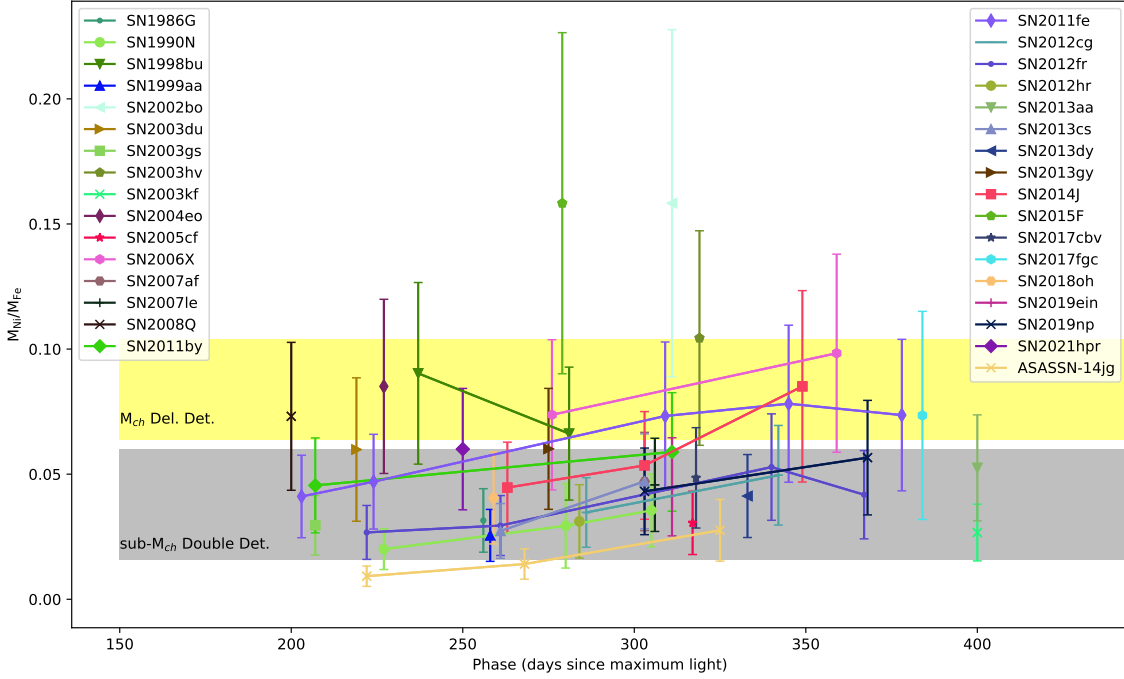


**Figure 4.** Inferred mass ratio of Ni and Fe as a function of phase after maximum light for SNe Ia collected in this work. Following Flörs et al. (2020), the prediction for the Ni/Fe ratio of DDT models locate in the yellow region (Seitenzahl et al. 2013) and that of sub- $M_{\text{Ch}}$  models locate in the gray region (Shen et al. 2018).

equal possibility to find a SNe Ia with redshifted or blueshifted nebular velocity; (2) About half red points have a normal Si II velocity ( $\lesssim 12000 \text{ km s}^{-1}$ ), which means SNe Ia displaying redshifted nebular velocity is not bound to a high Si II velocity; (3) A positive correlation between the Ni/Fe ratio and the Si II velocity is found for both the red points and blue points. If the viewing angles of all SNe Ia are the same value, we would expect that red points and blue points of Figure 5 were fully mixed just like Figure 6. We also notice that red points and blue point of Figure 5 tend to mix with each other when the Si II velocity is about  $10000 \text{ km s}^{-1}$ . For these SNe Ia, symmetric explosion models may be more suitable.

The correlation between the Ni/Fe ratio and  $\Delta m_{15}(B)$  showed in Figure 6 implies that the inferred Ni/Fe ratio may be an important parameter for SNe Ia just like  $\Delta m_{15}(B)$ . This correlation is reasonable. A higher Ni/Fe ratio means a higher ratio of stable-to-radioactive nucleosynthetic products. The radioactive  $^{56}\text{Ni}$  is an important energy source for the luminosity of SNe Ia at early time, so the potmaximum decline rate  $\Delta m_{15}(B)$  in-

creases with a higher of stable-to-radioactive nucleosynthetic products if the total quantity of nickel is similar. Although exceptions appear in the bottom right of Figure 6 that have a large  $\Delta m_{15}(B)$  and a low Ni/Fe ratio, they are 91bg-like SNe Ia which have less  $^{56}\text{Ni}$  compared to the normal SNe Ia and most are found in old stellar population (Panther et al. 2019) where the metallicity is low.

## 5.2. Calcium in the 7300 Å region

Whether calcium has a contribution to the 7300 Å region of the late-time SNe Ia spectrum has been discussed in many studies. Maguire et al. (2018) use the Bayesian Information Criterion to select between models with and without a contribution from calcium and the results are in favour of the no calcium models for their SNe Ia samples. Flörs et al. (2020) use the 19390 Å line to constrain the 7378 Å line for high SNR spectra and find the contribution of calcium is very limited in the 7300 Å region. However, Tucker et al. (2021) identify [Ca II] 7291 Å, 7324 Å doublet in the spectrum of SN 2011fe at about 480 days, where a central emission

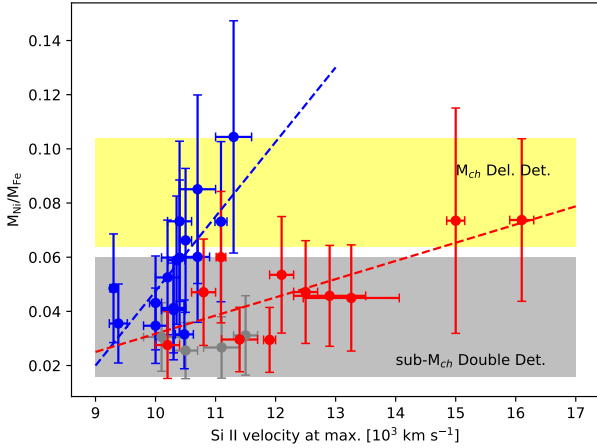


**Figure 5.** Inferred mass ratio of Ni and Fe vs. the Si II 6355 Å velocity at maximum. SNe Ia that have a redshifted (blueshifted) nebular velocity are plotted in red (blue). The SNe Ia plotted in gray have a zero nebular velocity under the uncertainty. The dashed lines are linear best-fits to the corresponding color points.

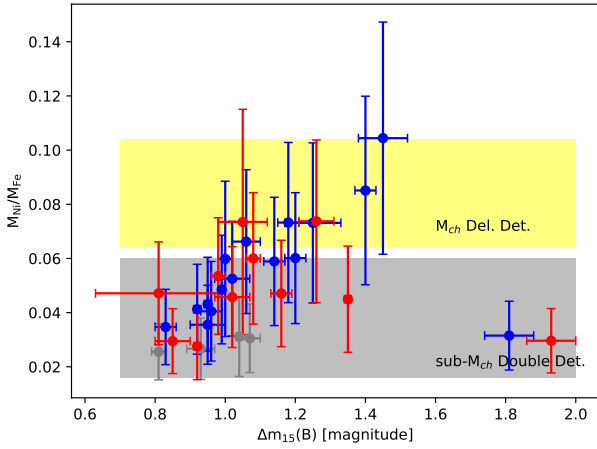


**Figure 6.** Inferred mass ratio of Ni and Fe vs. the decline rates  $\Delta m_{15}(B)$ . SNe Ia that have a redshifted (blueshifted) nebular velocity are plotted in red (blue). The SNe Ia plotted in gray have a zero nebular velocity under the uncertainty.

peak appears and the emission profile transitions from double- to triple-peaked (see Figure 1 in Tucker et al. 2021). And the nickel features measured from our multi-component Gaussian fits, where possible contribution of calcium is neglected, have overly-broad widths and much

more blueward shifts compared with the iron features in some cases. If the calcium is not negligible, this unexpected results would be understandable since the nickel features given by our fits would be the blended emission lines of nickel and calcium.

We have attempted to reduce the possible effect of calcium on our fits. We try to remove some data points of the spectrum before fitting when overly-broad nickel features appear. This is a crude but effective method in some cases (see the bottom panel of Figure 3). Nevertheless, there are only one spectrum which we have to use this method to avoid overly-broad nickel features in this work and our method is effective on it. Thus, the correlations found in section 4 are little affected. Note that we also remove some data points around 7300 Å of the spectra of SN 2017fgc and SN 2019ein due to the unexpected narrow emission whose source is unclear.

## 6. CONCLUSIONS

We have performed multi-component Gaussian fits to the 7300 Å [Fe II]/[Ni II]-dominated region for 33 SNe Ia collected in this work. This has allowed us to measure the velocity shifts and flux ratios of [Ni II] and [Fe II] features in this region, which can be used to infer Nebular velocities and late-time Ni/Fe ratios respectively. Connecting these inferred late-time parameters with the early-time observations (Si II velocity at maximum light and  $\Delta m_{15}(B)$ ), we find some interesting connections between them.

Our main results are:

(i) The majority (about 2/3) of SNe Ia in this work have a Ni/Fe ratio in the range of 0.02 - 0.06 with an uncertainty of more than 40 percent, in favour of sub- $M_{Ch}$  models.

(ii) Metallicity is one of the intrinsic sources of the diversity of Si II velocities while geometric effect caused by asymmetric explosion models affects the observed Si II velocity. For the SNe Ia that have a Si II velocity about 10000  $km s^{-1}$ , symmetric explosion models may be more suitable.

(iii) The Ni/Fe ratio has a positive correlation with  $\Delta m_{15}(B)$  except for 91bg-like SNe Ia which have a large  $\Delta m_{15}(B)$  and low metallicity environment.

(iv) Although a possible contribution of calcium cannot be completely ruled out, our results are little affected.

Connecting the early-time and late-time observations of SNe Ia allows us to understand the explosion mechanism better. In future work, more high-quality late-time spectra are needed to confirm these connections and find some new connections.

to be written

## REFERENCES

- Amanullah, R., Goobar, A., Johansson, J., et al. 2014, ApJL, 788, L21, doi: [10.1088/2041-8205/788/2/L21](https://doi.org/10.1088/2041-8205/788/2/L21)
- Anupama, G. C., Sahu, D. K., & Jose, J. 2005, A&A, 429, 667, doi: [10.1051/0004-6361:20041687](https://doi.org/10.1051/0004-6361:20041687)
- Benetti, S., Meikle, P., Stehle, M., et al. 2004, MNRAS, 348, 261, doi: [10.1111/j.1365-2966.2004.07357.x](https://doi.org/10.1111/j.1365-2966.2004.07357.x)
- Blondin, S., Matheson, T., Kirshner, R. P., et al. 2012, AJ, 143, 126, doi: [10.1088/0004-6256/143/5/126](https://doi.org/10.1088/0004-6256/143/5/126)
- Brown, P. J., Smitka, M. T., Wang, L., et al. 2015, ApJ, 805, 74, doi: [10.1088/0004-637X/805/1/74](https://doi.org/10.1088/0004-637X/805/1/74)
- Burgaz, U., Maeda, K., Kalomeni, B., et al. 2021, MNRAS, 502, 4112, doi: [10.1093/mnras/stab254](https://doi.org/10.1093/mnras/stab254)
- Burns, C. R., Stritzinger, M., Phillips, M. M., et al. 2014, ApJ, 789, 32, doi: [10.1088/0004-637X/789/1/32](https://doi.org/10.1088/0004-637X/789/1/32)
- Childress, M. J., Hillier, D. J., Seitzzahl, I., et al. 2015, MNRAS, 454, 3816, doi: [10.1093/mnras/stv2173](https://doi.org/10.1093/mnras/stv2173)
- Cristiani, S., Cappellaro, E., Turatto, M., et al. 1992, A&A, 259, 63
- Filippenko, A. V. 1997, ARA&A, 35, 309, doi: [10.1146/annurev.astro.35.1.309](https://doi.org/10.1146/annurev.astro.35.1.309)
- Flörs, A., Spyromilio, J., Taubenberger, S., et al. 2020, MNRAS, 491, 2902, doi: [10.1093/mnras/stz3013](https://doi.org/10.1093/mnras/stz3013)
- Foley, R. J., & Kasen, D. 2011, ApJ, 729, 55, doi: [10.1088/0004-637X/729/1/55](https://doi.org/10.1088/0004-637X/729/1/55)
- Foley, R. J., Fox, O. D., McCully, C., et al. 2014, MNRAS, 443, 2887, doi: [10.1093/mnras/stu1378](https://doi.org/10.1093/mnras/stu1378)
- Galbany, L., Moreno-Raya, M. E., Ruiz-Lapuente, P., et al. 2016, MNRAS, 457, 525, doi: [10.1093/mnras/stw026](https://doi.org/10.1093/mnras/stw026)
- Gao, J., Jiang, B. W., Li, A., Li, J., & Wang, X. 2015, ApJL, 807, L26, doi: [10.1088/2041-8205/807/2/L26](https://doi.org/10.1088/2041-8205/807/2/L26)
- Gomez, G., Lopez, R., & Sanchez, F. 1996, AJ, 112, 2094, doi: [10.1086/118166](https://doi.org/10.1086/118166)
- Graham, M. L., Kumar, S., Hosseinzadeh, G., et al. 2017, MNRAS, 472, 3437, doi: [10.1093/mnras/stx2224](https://doi.org/10.1093/mnras/stx2224)
- Graham, M. L., Kennedy, T. D., Kumar, S., et al. 2022, arXiv e-prints, arXiv:2201.07864, <https://arxiv.org/abs/2201.07864>
- Guillochon, J., Parrent, J., Kelley, L. Z., & Margutti, R. 2017, ApJ, 835, 64, doi: [10.3847/1538-4357/835/1/64](https://doi.org/10.3847/1538-4357/835/1/64)
- Hillebrandt, W., & Niemeyer, J. C. 2000, ARA&A, 38, 191, doi: [10.1146/annurev.astro.38.1.191](https://doi.org/10.1146/annurev.astro.38.1.191)
- Holmbo, S., Stritzinger, M. D., Shappee, B. J., et al. 2019, A&A, 627, A174, doi: [10.1051/0004-6361/201834389](https://doi.org/10.1051/0004-6361/201834389)
- Iben, I. J., & Tutukov, A. V. 1984, ApJS, 54, 335, doi: [10.1086/190932](https://doi.org/10.1086/190932)
- Im, M., Choi, C., Yoon, S.-C., et al. 2015, ApJS, 221, 22, doi: [10.1088/0067-0049/221/1/22](https://doi.org/10.1088/0067-0049/221/1/22)
- Iwamoto, K., Brachwitz, F., Nomoto, K., et al. 1999, ApJS, 125, 439, doi: [10.1086/313278](https://doi.org/10.1086/313278)
- Jerkstrand, A., Ergon, M., Smartt, S. J., et al. 2015, A&A, 573, A12, doi: [10.1051/0004-6361/201423983](https://doi.org/10.1051/0004-6361/201423983)
- Kawabata, M., Maeda, K., Yamanaka, M., et al. 2020, ApJ, 893, 143, doi: [10.3847/1538-4357/ab8236](https://doi.org/10.3847/1538-4357/ab8236)
- Krisciunas, K., Marion, G. H., Suntzeff, N. B., et al. 2009, AJ, 138, 1584, doi: [10.1088/0004-6256/138/6/1584](https://doi.org/10.1088/0004-6256/138/6/1584)
- Leloudas, G., Stritzinger, M. D., Sollerman, J., et al. 2009, A&A, 505, 265, doi: [10.1051/0004-6361/200912364](https://doi.org/10.1051/0004-6361/200912364)
- Lentz, E. J., Baron, E., Branch, D., Hauschildt, P. H., & Nugent, P. E. 2000, ApJ, 530, 966, doi: [10.1086/308400](https://doi.org/10.1086/308400)
- Li, W., Wang, X., Vinkó, J., et al. 2019, ApJ, 870, 12, doi: [10.3847/1538-4357/aaec74](https://doi.org/10.3847/1538-4357/aaec74)
- Maeda, K., Taubenberger, S., Sollerman, J., et al. 2010a, ApJ, 708, 1703, doi: [10.1088/0004-637X/708/2/1703](https://doi.org/10.1088/0004-637X/708/2/1703)
- Maeda, K., Benetti, S., Stritzinger, M., et al. 2010b, Nature, 466, 82, doi: [10.1038/nature09122](https://doi.org/10.1038/nature09122)
- Maguire, K., Taubenberger, S., Sullivan, M., & Mazzali, P. A. 2016, MNRAS, 457, 3254, doi: [10.1093/mnras/stv2991](https://doi.org/10.1093/mnras/stv2991)
- Maguire, K., Sim, S. A., Shingles, L., et al. 2018, MNRAS, 477, 3567, doi: [10.1093/mnras/sty820](https://doi.org/10.1093/mnras/sty820)
- Maoz, D., Mannucci, F., & Nelemans, G. 2014, ARA&A, 52, 107, doi: [10.1146/annurev-astro-082812-141031](https://doi.org/10.1146/annurev-astro-082812-141031)
- Nomoto, K., Iwamoto, K., & Kishimoto, N. 1997a, Science, 276, 1378, doi: [10.1126/science.276.5317.1378](https://doi.org/10.1126/science.276.5317.1378)
- Nomoto, K., Iwamoto, K., Nakasato, N., et al. 1997b, NuPhA, 621, 467, doi: [10.1016/S0375-9474\(97\)00291-1](https://doi.org/10.1016/S0375-9474(97)00291-1)
- Pan, Y. C., Foley, R. J., Kromer, M., et al. 2015, MNRAS, 452, 4307, doi: [10.1093/mnras/stv1605](https://doi.org/10.1093/mnras/stv1605)
- Panther, F. H., Seitzzahl, I. R., Ruitter, A. J., et al. 2019, PASA, 36, e031, doi: [10.1017/pasa.2019.24](https://doi.org/10.1017/pasa.2019.24)
- Pastorello, A., Taubenberger, S., Elias-Rosa, N., et al. 2007, MNRAS, 376, 1301, doi: [10.1111/j.1365-2966.2007.11527.x](https://doi.org/10.1111/j.1365-2966.2007.11527.x)
- Phillips, M. M., Phillips, A. C., Heathcote, S. R., et al. 1987, PASP, 99, 592, doi: [10.1086/132020](https://doi.org/10.1086/132020)
- Phillips, M. M., Simon, J. D., Morrell, N., et al. 2013, ApJ, 779, 38, doi: [10.1088/0004-637X/779/1/38](https://doi.org/10.1088/0004-637X/779/1/38)
- Schlaflly, E. F., & Finkbeiner, D. P. 2011, ApJ, 737, 103, doi: [10.1088/0004-637X/737/2/103](https://doi.org/10.1088/0004-637X/737/2/103)



- Seitenzahl, I. R., Ciaraldi-Schoolmann, F., Röpke, F. K., et al. 2013, *MNRAS*, 429, 1156, doi: [10.1093/mnras/sts402](https://doi.org/10.1093/mnras/sts402)
- Shappee, B. J., Piro, A. L., Stanek, K. Z., et al. 2018, *ApJ*, 855, 6, doi: [10.3847/1538-4357/aaa1e9](https://doi.org/10.3847/1538-4357/aaa1e9)
- Shen, K. J., Kasen, D., Miles, B. J., & Townsley, D. M. 2018, *ApJ*, 854, 52, doi: [10.3847/1538-4357/aaa8de](https://doi.org/10.3847/1538-4357/aaa8de)
- Silverman, J. M., Ganeshalingam, M., & Filippenko, A. V. 2013, *MNRAS*, 430, 1030, doi: [10.1093/mnras/sts674](https://doi.org/10.1093/mnras/sts674)
- Silverman, J. M., Ganeshalingam, M., Cenko, S. B., et al. 2012, *ApJL*, 756, L7, doi: [10.1088/2041-8205/756/1/L7](https://doi.org/10.1088/2041-8205/756/1/L7)
- Sim, S. A., Röpke, F. K., Hillebrandt, W., et al. 2010, *ApJL*, 714, L52, doi: [10.1088/2041-8205/714/1/L52](https://doi.org/10.1088/2041-8205/714/1/L52)
- Srivastav, S., Ninan, J. P., Kumar, B., et al. 2016, *MNRAS*, 457, 1000, doi: [10.1093/mnras/stw039](https://doi.org/10.1093/mnras/stw039)
- Stahl, B. E., Zheng, W., de Jaeger, T., et al. 2020, *MNRAS*, 492, 4325, doi: [10.1093/mnras/staa102](https://doi.org/10.1093/mnras/staa102)
- Stanishev, V., Goobar, A., Benetti, S., et al. 2007, *A&A*, 469, 645, doi: [10.1051/0004-6361:20066020](https://doi.org/10.1051/0004-6361:20066020)
- Suntzeff, N. B., Phillips, M. M., Covarrubias, R., et al. 1999, *AJ*, 117, 1175, doi: [10.1086/300771](https://doi.org/10.1086/300771)
- Timmes, F. X., Brown, E. F., & Truran, J. W. 2003, *ApJL*, 590, L83, doi: [10.1086/376721](https://doi.org/10.1086/376721)
- Tucker, M. A., Ashall, C., Shappee, B. J., et al. 2021, arXiv e-prints, arXiv:2111.00016. <https://arxiv.org/abs/2111.00016>
- Tucker, M. A., Shappee, B. J., & Wisniewski, J. P. 2019, *ApJL*, 872, L22, doi: [10.3847/2041-8213/ab0286](https://doi.org/10.3847/2041-8213/ab0286)
- Wang, L., Contreras, C., Hu, M., et al. 2020, *ApJ*, 904, 14, doi: [10.3847/1538-4357/abba82](https://doi.org/10.3847/1538-4357/abba82)
- Wang, X., Chen, J., Wang, L., et al. 2019, *ApJ*, 882, 120, doi: [10.3847/1538-4357/ab26b5](https://doi.org/10.3847/1538-4357/ab26b5)
- Wang, X., Wang, L., Filippenko, A. V., Zhang, T., & Zhao, X. 2013, *Science*, 340, 170, doi: [10.1126/science.1231502](https://doi.org/10.1126/science.1231502)
- Wang, X., Li, W., Filippenko, A. V., et al. 2008, *ApJ*, 675, 626, doi: [10.1086/526413](https://doi.org/10.1086/526413)
- Webbink, R. F. 1984, *ApJ*, 277, 355, doi: [10.1086/161701](https://doi.org/10.1086/161701)
- Whelan, J., & Iben, Icko, J. 1973, *ApJ*, 186, 1007, doi: [10.1086/152565](https://doi.org/10.1086/152565)
- Yaron, O., & Gal-Yam, A. 2012, *PASP*, 124, 668, doi: [10.1086/666656](https://doi.org/10.1086/666656)
- Zeng, X., Wang, X., Esamdin, A., et al. 2021, *ApJ*, 919, 49, doi: [10.3847/1538-4357/ac0e9c](https://doi.org/10.3847/1538-4357/ac0e9c)
- Zhang, K., Wang, X., Zhang, J., et al. 2018, *MNRAS*, 481, 878, doi: [10.1093/mnras/sty2289](https://doi.org/10.1093/mnras/sty2289)
- Zhao, X., Wang, X., Maeda, K., et al. 2015, *ApJS*, 220, 20, doi: [10.1088/0067-0049/220/1/20](https://doi.org/10.1088/0067-0049/220/1/20)
- Zheng, W., Silverman, J. M., Filippenko, A. V., et al. 2013, *ApJL*, 778, L15, doi: [10.1088/2041-8205/778/1/L15](https://doi.org/10.1088/2041-8205/778/1/L15)

## APPENDIX

## A. OVERVIEW OF SNE Ia AND FITTING RESULTS

Table A1 presents basic information of SNe Ia in this work. Table A2 presents the SNe Ia whose  $R_v$  is not assumed to be 3.1. Figure A1 shows the fitting results for all spectra in this work and the corresponding parameters are presented in Table A3.

**Table A1.** SNe Ia light curve and spectral parameters, host galaxy information, number of late-time spectra and the corresponding phases.

Name	Host galaxy	Redshift	E(B-V)	$\Delta m_{15}(B)$	$v_0(\text{Si II})$	$N_{\text{spec}}$	Phase	Ref.	Ref.	Ref.
			(mag)	(mag)	1000 km s <sup>-1</sup>		d	$v_0(\text{Si II})$	$\Delta m_{15}(B)$	E(B-V)
SN1986G	NGC 5128	0.001825	1.1	1.81±0.07	10.00±0.15	1	256	1	2	3
SN1990N	NGC 4639	0.003369	0.02	0.95±0.05	10.53±0.15	3	227-305	1	4	5,6
SN1998bu	NGC 3368	0.002992	0.34	1.06±0.04	10.50±0.10	2	237, 281	7	7	9
SN1999aa	NGC 2595	0.014907	0.03	0.81±0.02	10.50±0.20	1	256	7	7	5,6
SN2002bo	NGC 3190	0.0043	0.43	1.15±0.03	13.20±0.20	1	311	7	7	9
SN2003du	UGC 9391	0.006408	0.01	1.00±0.02	10.40±0.30	1	219	7	7	10
SN2003gs	NGC 936	0.00477	0.07	1.93±0.07	11.40±0.30	1	207	7	7	11
SN2003hv	NGC 1201	0.005624	-0.03	1.45±0.07	11.30±0.30	1	319	7	7	2,6,12
SN2003kf	PGC 18373	0.00739	0.27	0.93±0.04	11.10±0.30	1	400	7	7	5,6
SN2004eo	NGC 6928	0.015718	0.23	1.40±0.03	10.70±0.30	1	227	7	7	5,6,13
SN2006X	NGC 4321	0.005294	1.42	1.26±0.05	16.10±0.20	2	276, 359	7	7	14
SN2007af	NGC 5584	0.005464	0.21	1.16±0.03	10.80±0.20	1	303	7	7	2,6,13
SN2007le	NGC 7721	0.006721	0.37	1.02±0.05	12.90±0.60	1	306	7	7	15
SN2008Q	NGC 524	0.0081	0.07	1.25±0.08	11.09±0.10	1	200	16	16	5,6
SN2011by	NGC 3972	0.002843	0.01	1.14±0.03	10.35±0.14	2	207, 311	16	16	5,6
SN2011fe	NGC 5457	0.000804	0.01	1.18±0.03	10.40±0.20	5	203-378	7	7	5,6
SN2012cg	NGC 4424	0.001458	0.20	0.83±0.03	10.00±0.20	2	286, 342	17	4	5,6,18
SN2012fr	NGC 1365	0.004	0.03	0.85±0.05	12.00±0.20	4	222-367	17	7	5,6
SN2012hr	PGC 18880	0.008	0.04	1.04±0.01	11.50±0.20	1	284	19	19	5,6
SN2013aa	NGC 5643	0.003999	0.21	0.95±0.01	10.20±0.20	1	400	19	19	5,6
SN2013cs	ESO576-17	0.00924	0.08	0.81±0.18	12.50±0.20	2	261, 303	19	19	5,6
SN2013dy	NGC 7250	0.00389	0.28	0.92±0.01	10.30±0.20	1	333,	20	4	5,6,21
SN2013gy	NGC 1418	0.014023	0.155	1.20±0.03	10.70±0.20	1	275	19	4	5,6,22
SN2014J	NGC 3034	0.000677	1.19	0.98±0.02	12.10±0.20	3	263-349	7	7	23
SN2015F	NGC 2422	0.0049	0.21	1.18±0.02	10.10±0.20	1	295	19	19	5,6,24
SN2017cbv	NGC 5643	0.003999	0.16	0.99±0.01	9.30±0.06	1	318	25	26	5,6
SN2017fgc	NGC 0474	0.001458	0.20	1.05±0.07	15.20±0.20	1	384	27	27	5,6,27
SN2018oh	UGC 04780	0.012	0.04	0.96±0.03	10.10±0.10	1	259	28	28	5,6
SN2019ein	NGC 5353	0.007755	0.1	1.35±0.01	14.00±0.20	1	311	29	29	5,6,30
SN2019np	NGC 3254	0.00452	0.12	1.04±0.04	10.00±0.10	2	303, 368	31	31	5,6,31
SN2021hpr	NGC 3147	0.009346	0.1	1.08±0.02	11.09±0.08	1	250	?	?	?

**Table A1** *continued*

**Table A1** (*continued*)

Name	Host galaxy	Redshift	E(B-V)	$\Delta m_{15}(B)$	$v_0(\text{Si II})$	$N_{\text{spec}}$	Phase	Ref.	Ref.	Ref.
			(mag)	(mag)	1000 km s <sup>-1</sup>		d	$v_0(\text{Si II})$	$\Delta m_{15}(B)$	E(B-V)
ASASSN-14jg	PGC128348	0.014827	0.01	0.92±0.01	10.30±0.20	3	222-325	19	19	5,6

NOTE—Reference: (1) [Foley & Kasen \(2011\)](#); (2) [Cristiani et al. \(1992\)](#); (3) [Phillips et al. \(1987\)](#); (4) [Zhao et al. \(2015\)](#); (5) [Schlafly & Finkbeiner \(2011\)](#); (6) [Guillochon et al. \(2017\)](#); (7) [Wang et al. \(2019\)](#); (8) [Suntzeff et al. \(1999\)](#); (9) [Benetti et al. \(2004\)](#); (10) [Anupama et al. \(2005\)](#); (11) [Krisciunas et al. \(2009\)](#); (12) [Leloudas et al. \(2009\)](#); (13) [Burns et al. \(2014\)](#); (14) [Wang et al. \(2008\)](#); (15) [Phillips et al. \(2013\)](#); (16) [Silverman et al. \(2013\)](#); (17) [Maguire et al. \(2018\)](#); (18) [Silverman et al. \(2012\)](#); (19) [Graham et al. \(2017\)](#); (20) [Pan et al. \(2015\)](#); (21) [Zheng et al. \(2013\)](#); (22) [Holmbo et al. \(2019\)](#); (23) [Foley et al. \(2014\)](#); (24) [Im et al. \(2015\)](#); (25) [Graham et al. in prep](#); (26) [Wang et al. \(2020\)](#); (27) [Zeng et al. \(2021\)](#); (28) [Li et al. \(2019\)](#); (29) [Xi et al. in prep](#); (30) [Kawabata et al. \(2020\)](#); (31) [Sai et al. in prep](#).

**Table A2.**  $R_v$  values and references of SNe Ia whose  $R_v$  values are not assumed to be 3.1.

Name	$R_v$	Ref.
SN2006X	1.5	<a href="#">Wang et al. (2008)</a> ; <a href="#">Phillips et al. (2013)</a> ; <a href="#">Burns et al. (2014)</a>
SN2014J	1.5	<a href="#">Amanullah et al. (2014)</a> ; <a href="#">Foley et al. (2014)</a> ; <a href="#">Gao et al. (2015)</a> ; <a href="#">Brown et al. (2015)</a>
SN2017fgc	1.5	<a href="#">Burgaz et al. (2021)</a>
SN2019ein	1.5	<a href="#">Kawabata et al. (2020)</a>

**Table A3.** Multi-component Gaussian fits parameters of nebular-phase emission lines and their inferred nebular velocities and Ni/Fe ratios.

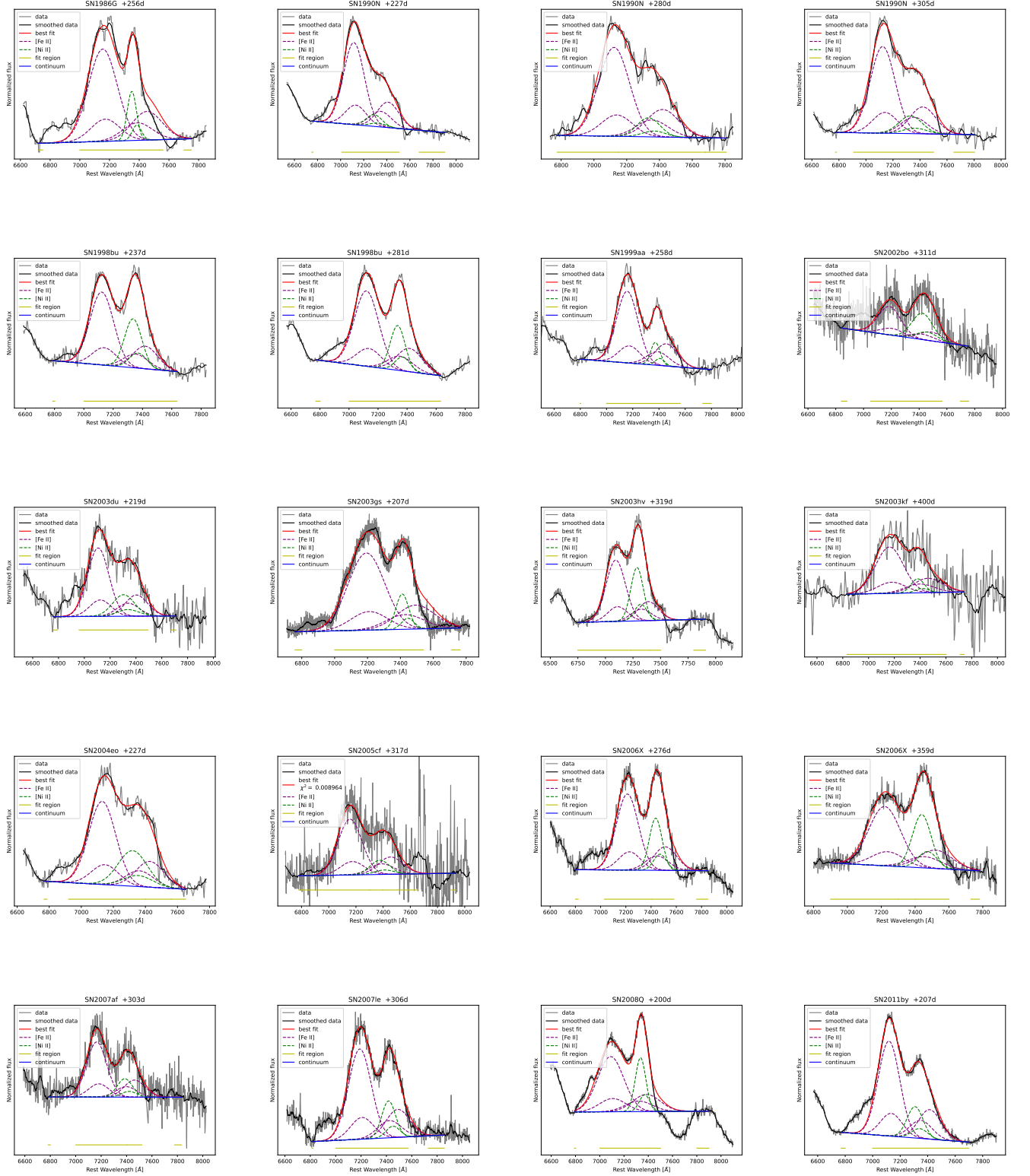
Name	Phase	[Fe II] Velocity	[Ni II] Velocity	[Fe II] FWHM	[Ni II] FWHM	Flux ratio	Nebular Vel.	Inferred	Ref.
	[days]	[km s <sup>-1</sup> ]	[km s <sup>-1</sup> ]	[km s <sup>-1</sup> ]	[km s <sup>-1</sup> ]	Ni/Fe	[km s <sup>-1</sup> ]	Ni/Fe	Spec.
SN1986G	256	-17±244	-1133±263	9614±158	2979±306	0.170±0.008	-575±179	0.032±0.013	1
SN1990N	227	-1691±241	-3581±427	8933±213	6506±149	0.108±0.008	-2636±245	0.020±0.008	2
SN1990N	280	-1350±375	-1821±916	9330±390	6690±1307	0.158±0.065	-1586±495	0.029±0.017	2
SN1990N	305	-1312±234	-1961±459	9075±131	8217±352	0.192±0.018	-1637±257	0.036±0.015	2
SN1998bu	237	-1379±248	-1704±287	8007±241	5642±305	0.487±0.019	-1542±190	0.090±0.036	BSNIP
SN1998bu	281	-1455±260	-1732±308	8325±144	4861±359	0.357±0.011	-1594±202	0.066±0.027	BSNIP
SN1999aa	258	115±265	-209±279	8077±106	3402±221	0.138±0.010	-46±192	0.026±0.010	BSNIP
SN2002bo	311	1324±260	1823±421	8063±1171	7194±229	0.854±0.153	1573±247	0.158±0.069	3
SN2003du	219	-1994±292	-3010±735	8159±356	8121±812	0.323±0.085	-2502±395	0.060±0.029	6
SN2003gs	207	1604±234	1356±256	10954±243	3709±25	0.160±0.006	1480±173	0.030±0.012	BSNIP
SN2003hv	319	-2582±246	-3716±315	8688±204	5462±562	0.563±0.052	-3149±200	0.104±0.043	7
SN2003kf	400	304±396	117±729	10732±214	4962±1596	0.144±0.021	210±415	0.027±0.011	CfA
SN2004eo	227	-1029±247	-2346±348	8363±149	8699±316	0.459±0.039	-1688±213	0.085±0.035	8
SN2005cf	317	216±444	308±537	9055±250	5808±274	0.165±0.018	262±348	0.031±0.013	BSNIP
SN2006X	276	2379±273	2383±263	8586±323	4833±60	0.398±0.030	2381±189	0.074±0.030	BSNIP
SN2006X	359	2740±235	2496±245	9238±214	5291±73	0.531±0.024	2618±170	0.098±0.040	BSNIP
SN2007af	303	402±227	332±363	7787±387	5748±247	0.254±0.030	367±214	0.047±0.020	CfA

**Table A3** *continued*

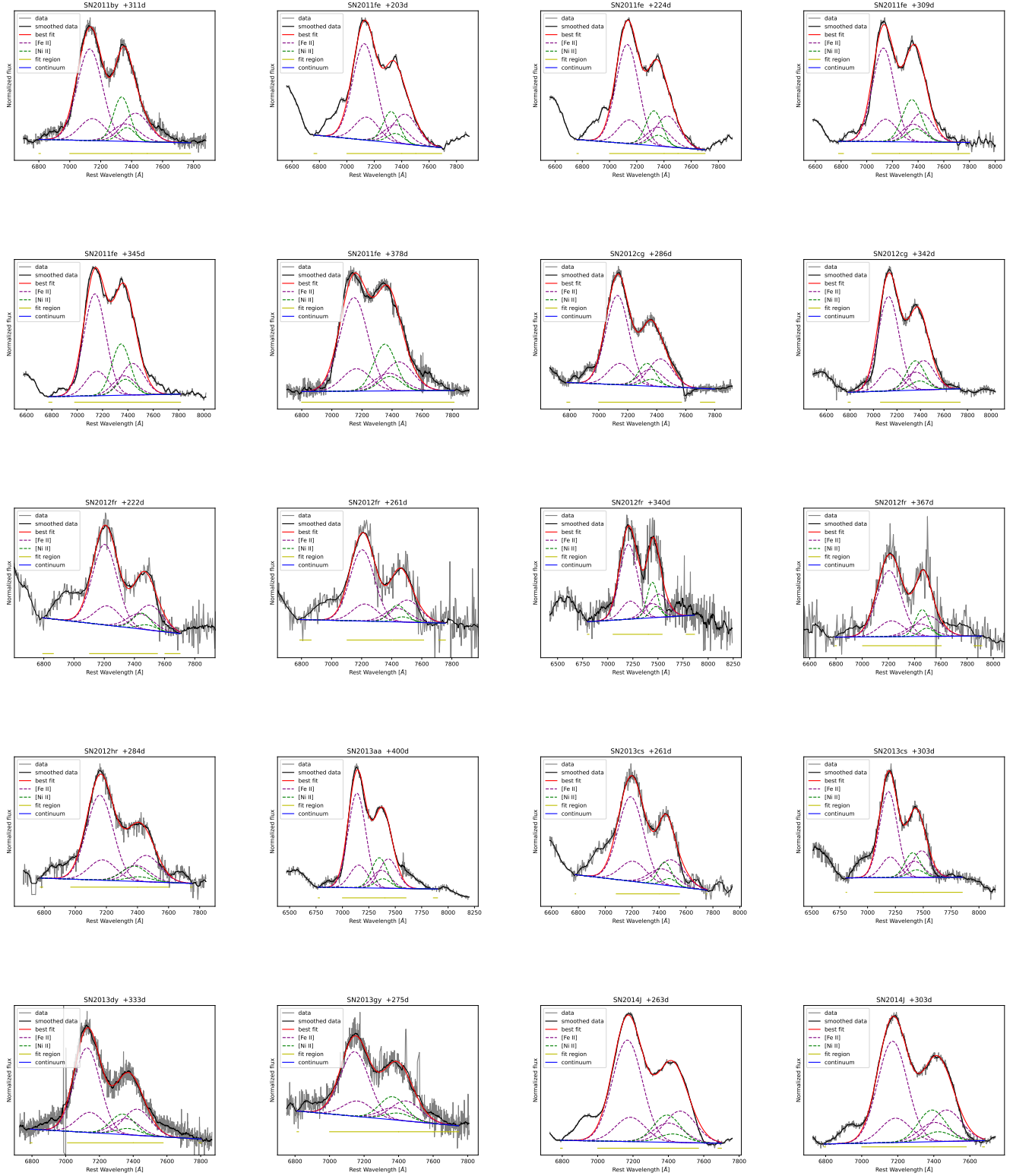
Table A3 (*continued*)

Name	Phase	[Fe II] Velocity	[Ni II] Velocity	[Fe II] FWHM	[Ni II] FWHM	Flux ratio	Nebular Vel.	Inferred	Ref.
	[days]	[km s <sup>-1</sup> ]	[km s <sup>-1</sup> ]	[km s <sup>-1</sup> ]	[km s <sup>-1</sup> ]	Ni/Fe	[km s <sup>-1</sup> ]	Ni/Fe	Spec.
SN2007le	306	1481±248	1599±297	8872±296	5204±78	0.247±0.019	1540±193	0.046±0.019	BSNIP
SN2008Q	200	-2730±309	-1697±221	10661±227	4183±82	0.394±0.023	-2213±190	0.073±0.030	BSNIP
SN2011by	207	-1531±277	-2830±485	7718±281	5568±439	0.246±0.029	-2181±279	0.046±0.019	9
SN2011by	311	-1064±212	-1711±242	8016±158	5099±40	0.318±0.013	-1387±161	0.059±0.024	9
SN2011fe	203	-1141±210	-2210±238	8473±75	5629±54	0.222±0.007	-1675±158	0.041±0.016	10
SN2011fe	224	-1026±229	-2070±308	8195±130	5732±146	0.254±0.012	-1548±192	0.047±0.019	10
SN2011fe	309	-1066±250	-1076±331	8379±218	7106±225	0.395±0.022	-1071±207	0.073±0.030	10
SN2011fe	345	-638±251	-1295±284	8558±109	6955±128	0.422±0.014	-966±189	0.078±0.031	10
SN2011fe	378	-340±296	-1047±355	9109±292	7014±225	0.397±0.038	-693±231	0.074±0.030	10
SN2012cg	286	-1069±223	-1825±354	7857±169	5625±95	0.187±0.005	-1447±209	0.035±0.014	11
SN2012cg	342	-1109±234	-840±315	8771±106	7316±148	0.267±0.010	-974±196	0.050±0.020	12
SN2012fr	222	2047±265	2939±400	8078±97	5672±159	0.144±0.007	2493±240	0.027±0.011	13
SN2012fr	261	2052±230	2510±495	8064±1133	5262±95	0.159±0.012	2281±273	0.029±0.012	13
SN2012fr	340	2116±242	2686±236	8689±257	5086±61	0.285±0.013	2401±169	0.053±0.021	13
SN2012fr	367	2130±267	3263±252	9212±1022	4961±440	0.225±0.030	2697±184	0.042±0.018	13
SN2012hr	284	133±241	71±649	8392±357	7594±891	0.168±0.042	102±346	0.031±0.015	13
SN2013aa	400	-738±238	-1150±262	8181±120	6999±226	0.283±0.014	-944±177	0.053±0.021	14
SN2013cs	261	1477±234	2634±247	9293±68	4854±74	0.147±0.003	2055±170	0.027±0.011	14
SN2013cs	303	1352±247	1130±368	7847±166	6717±165	0.254±0.011	1241±221	0.047±0.019	12
SN2013dy	333	-1169±224	-1629±260	7600±78	6787±229	0.223±0.009	-1399±171	0.041±0.017	15
SN2013gy	275	-389±211	-533±427	8140±218	7166±170	0.324±0.013	-461±238	0.060±0.024	13
SN2014J	263	550±217	595±312	8313±133	7224±253	0.241±0.018	572±190	0.045±0.018	10
SN2014J	303	664±222	485±333	8072±135	7222±143	0.289±0.012	574±200	0.053±0.022	10
SN2014J	349	628±312	929±312	8517±520	8847±1027	0.459±0.094	779±220	0.085±0.038	17
SN2015F	279	-549±303	-1245±255	7304±157	9769±812	0.854±0.136	-897±198	0.158±0.068	14
SN2017cbv	318	-815±366	-1714±443	7764±423	7221±347	0.262±0.027	-1265±287	0.049±0.020	19
SN2017fgc	384	3539±1287	3497±3423	9272±1682	6376±2340	0.362±0.164	3518±1828	0.069±0.042	20
SN2018oh	259	-1847±375	-3910±804	7052±342	5319±666	0.218±0.047	-2878±444	0.041±0.018	19
SN2019ein	311	1665±2974	2473±770	11151±6624	3745±1376	0.334±0.191	2069±1536	0.064±0.045	21
SN2019np	303	-1695±226	-3240±410	7014±81	5542±241	0.233±0.008	-2467±234	0.043±0.017	22
SN2019np	368	-1522±317	-3042±401	7165±333	5662±77	0.305±0.018	-2282±256	0.057±0.023	22
SN2021hpr	250	852±229	279±552	7734±933	5307±730	0.324±0.019	565±299	0.060±0.024	This work
ASASSN-14jg	222	1335±235	1389±383	8397±261	2763±289	0.050±0.009	1362±225	0.009±0.004	19
ASASSN-14jg	268	1609±235	1071±355	7832±238	4207±339	0.076±0.012	1340±213	0.014±0.006	14
ASASSN-14jg	325	1769±255	2335±277	8774±664	5010±93	0.149±0.030	2052±188	0.028±0.012	23

NOTE—Reference: (1) Cristiani et al. (1992); (2) Gomez et al. (1996); (3) Blondin et al. (2012); (4) Stanishev et al. (2007); (5) Leloudas et al. (2009); (6) Pastorello et al. (2007); (7) Silverman et al. (2013); (8) Stahl et al. (2020) (9) Shappee et al. (2018) (10) Maguire et al. (2016); (11) Childress et al. (2015); (12) Graham et al. (2017); (13) Pan et al. (2015); (14) Galbany et al. (2016); (15) Srivastav et al. (2016); (16) Zhang et al. (2018); (17) Tucker et al. (2019); (18) Zeng et al. (2021); (19) Xi et al., in prep; (20) Maguire et al. (2018); (21) Xi et al., in prep (22) Sai et al., in prep.







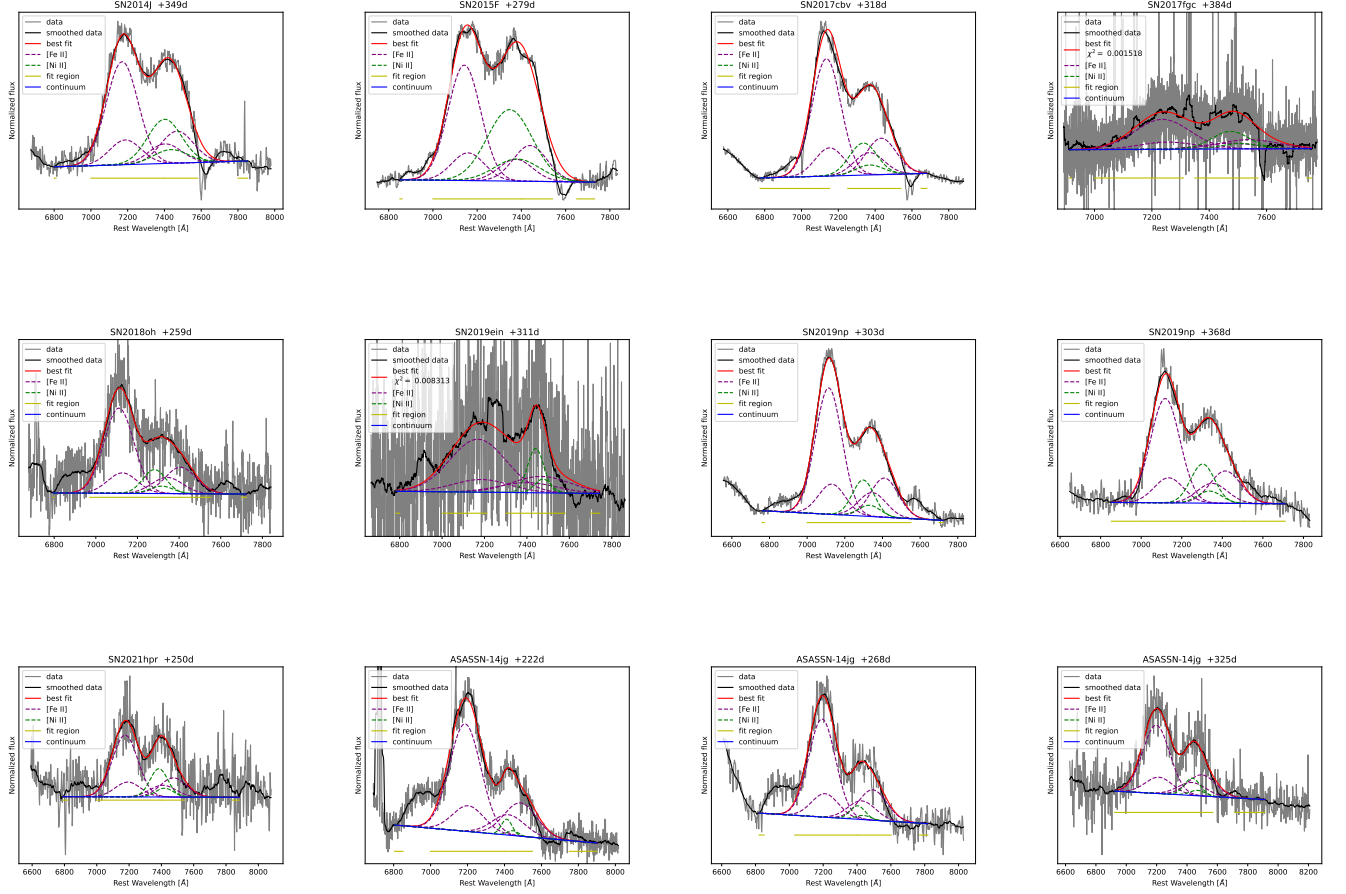


**Figure A1.** Best fits to the 7300 Å region for all samples in this work. The reddening corrected observed spectra are shown in gray while the smoothed spectra are shown in black. The overall fits are shown in red, the [Fe II] features are showed in purple dashed lines and the [Ni II] features are showed in green dashed lines. The yellow lines show the region we choose to fit. The continuums are showed in blue.